Solution Structure and Dynamics of the Human−*Escherichia coli* Thioredoxin Chimera: Insights into Thermodynamic Stability[†,‡]

Bindi Dangi, Anatoliy V. Dobrodumov, John M. Louis, and Angela M. Gronenborn*

Laboratory of Chemical Physics, National Institute of Diabetes and Digestive and Kidney Diseases, National Institutes of Health, Bethesda, Maryland 20892-0560

Received March 21, 2002; Revised Manuscript Received May 31, 2002

ABSTRACT: We have determined the high-resolution solution structure of the oxidized form of a chimeric human and *Escherichia coli* thioredoxin (TRX_{HE}) by NMR. The overall structure is well-defined with a rms difference for the backbone atoms of 0.27 ± 0.06 Å. The topology of the protein is identical to those of the human and *E. coli* parent proteins, consisting of a central five-stranded β-sheet surrounded by four α-helices. Analysis of the interfaces between the two domains derived from the human and *E. coli* sequences reveals that the general hydrophobic packing is unaltered and only subtle changes in the details of side chain interactions are observed. The packing of helix α_4 with helix α_2 across the hybrid interface is less optimal than in the parent molecules, and electrostatic interactions between polar side chains are missing. In particular, lysine−glutamate salt bridges between residues on helices α_2 and α_4, which were observed in both human and *E. coli* proteins, are not present in the chimeric protein. The origin of the known reduced thermodynamic stability of TRX_{HE} was probed by mutagenesis on the basis of these structural findings. Two mutants of TRX_{HE}, S44D and S44E, were created, and their thermal and chemical stabilities were examined. Improved stability toward chaotropic agents was observed for both mutants, but no increase in the denaturation temperature was seen compared to that of TRX_{HE}. In addition to the structural analysis, the backbone dynamics of TRX_{HE} were investigated by ^{15}N NMR relaxation measurements. Analysis using the model free approach reveals that the protein is fairly rigid with an average S^2 of 0.88. Increased mobility is primarily present in two external loop regions comprising residues 72−74 and 92−94 that contain glycine and proline residues.

Thioredoxin is a protein molecule that is found in essentially all organisms, and its main function involves redox catalysis (*1*). Three-dimensional structures of several thioredoxins from a variety of sources have been determined, by either X-ray crystallography or NMR[1] (*2*−*8*). All thioredoxins share very similar three-dimensional structures, comprising a central core of five β-strands, surrounded by four α-helices. For a variety of reasons, thioredoxin has long been employed as a model system for studying protein folding and stability (*9*−*14*). It is small (~107 residues) and very stable and has been investigated in a large number of different laboratories. This has led to a thorough structural, thermodynamic, and kinetic characterization of this protein family. Recently, we created a chimeric thioredoxin comprising human (residues 1−67) and *Escherichia coli* sequences (residues 68−107) (*9*). The amino acid sequence of this chimera, a sequence comparison between human and *E. coli* thioredoxins, and the three-dimensional fold of TRX_{HE} are provided in Figure 1. A 25% level of sequence identity exists between the human and *E. coli* proteins (*1*), and the three-dimensional structures differ by only 1.6 Å for the backbone atom positions (*4*). Biophysical and biochemical characterization of this hybrid has previously revealed that its thermodynamic stability is reduced compared to the stabilities of the two parent proteins, both with respect to chemical and thermal denaturation (*9*).

To date, no general rule as to which factors lead to increased protein stability has emerged, except that cumulative effects of hydrogen bonding, electrostatic interactions, better hydrophobic internal packing, helix−dipole stabilization, enhanced stability of secondary structure elements, etc., all come into play. Indeed, despite extensive sets of mutants in some protein systems, it frequently is difficult to pinpoint the exact cause of a change in stability. Proteins keep surprising us, and protein stability can be influenced by very subtle structural effects. The present hybrid thioredoxin thus seemed to be an ideal system for a detailed analysis aimed at elucidating some of the structural factors that affect its stability. We therefore determined the NMR solution structure to high resolution.

In addition to questions concerning protein structure and stability, the hybrid thioredoxin allows us to also probe issues regarding protein−protein recognition. To dissect and un-

[†] This work was supported in part by the Intramural AIDS Targeted Antiviral Program of the Office of the Director of the National Institutes of Health (A.M.G.).

[‡] PDB entry XXXX. BMRB accession code 5308.

* To whom correspondence should be addressed: Bldg. 5, Room 130, NIH, Bethesda, MD 20892. Phone: (301) 496-5414. Fax: (301) 496-1690. E-mail: gronenborn@nih.gov.

[1] Abbreviations: TRX, thioredoxin; TRX_{HE}, hybrid human−*E. coli* thioredoxin chimera; NMR, nuclear magnetic resonance; HSQC, heteronuclear single-quantum correlation; NOE, nuclear Overhauser effect; $^{15}N\{^1H\}$NOE, $^1H-^{15}N$ steady state heteronuclear NOE; GdnHCl, guanidine hydrochloride; CD, circular dichroism; EDTA, ethylenediaminetetraacetic acid.

10.1021/bi0258501
Published on Web 06/29/2002

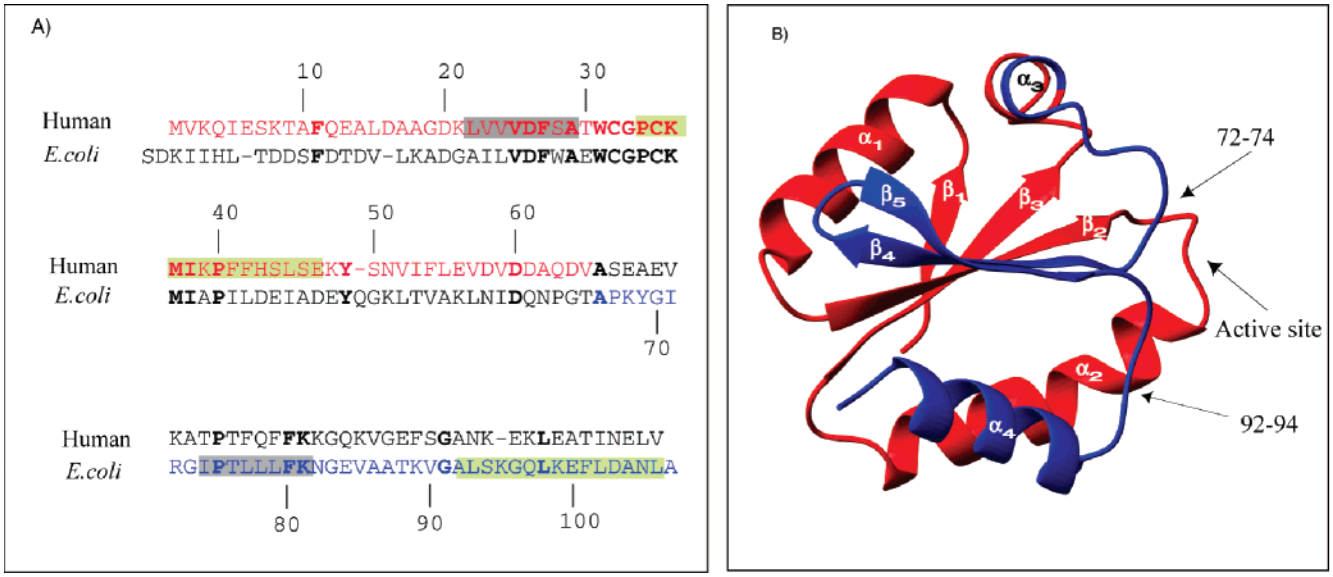

FIGURE 1: (A) Sequence alignment of human and *E. coli* thioredoxins. The hybrid human−*E. coli* thioredoxin comprises residues 1−66 (red) derived from the human sequence and residues 67−107 (blue) from the *E. coli* sequence. Conserved residues are shown in bold. Amino acids at the $\beta_2-\beta_4$ and $\alpha_2-\alpha_4$ interfaces are highlighted in gray and green, respectively. (B) Ribbon representation of the TRX_{HE} structure. Regions of the structure comprising human and *E. coli* sequences are colored red and blue, respectively.

derstand the complexity of specific interactions within proteins, numerous mutagenesis studies have been carried out over the past decade, resulting in a large body of data relating the specific packing of amino acid residues in the hydrophobic cores of natural proteins to protein stability. Complementary to these mutagenesis studies were efforts aimed at ab initio protein design. Whereas the initial design efforts were marred by their inability to yield proteins with well-ordered tertiary structures, lately, considerable attention has been paid to side chain packing which in turn led to the successful generation of novel proteins. Despite this wealth of data, several aspects of molecular recognition are still obscure, and studies on well-defined model systems are invaluable. Consistent with thioredoxin's role as a model system, the newly created interface in the chimeric thioredoxin can be examined as a basic example of protein−protein interactions. In general, intermolecular domain interactions are very similar to intramolecular ones (*15*), and as such, the present system represents a unique opportunity. Intrachain domain−domain interfaces constitute ideal templates for studying the physical and chemical determinants that link structure and stability of polypeptides. In this regard, results obtained with complementary protein fragments have contributed substantially to our understanding of protein folding and design. A major difference in the forces that drive protein folding versus those that are responsible for complex formation is that protein folding is associated with a significantly larger loss in configurational entropy compared to the loss of translational, rotational, and side chain entropy upon protein−protein association. Thus, forces that drive complex formation are generally smaller than those that drive protein folding (*16*). For *E. coli* thioredoxin, it has been reported that different protein fragments (residues 1−37, 38−73, and 74−108) can recognize each other and assemble in solution to assume the thioredoxin fold (*17*). In particular, peptides comprising residues 1−73 and 74−108 associate and fold with a K_d of 49 nM (*12*), resulting in a stable complex, while those comprising residues 1−37 and 38−108 yield an unstable structure. According to all the available data, folding and assembly of *E. coli* thioredoxin involve association of β-strands β_2 and β_4. Our hybrid protein contains a new pairing for these two β-strands, since strand β_2 contains the human sequence and strand β_4 the *E. coli* sequence. This allowed us to investigate details of structural tolerance. In addition, the structural reasons for the reduced thermodynamic stability of the hybrid protein were elucidated. Indeed, the chimeric thioredoxin molecule is ideally suited for testing strategies aimed at evolving more stable protein interfaces. These studies may eventually lead to the design of interface targets preventing protein−protein association.

EXPERIMENTAL PROCEDURES

Sample Preparation. The hybrid human−*E. coli* thioredoxin (TRX_{HE}) was expressed using the BL21(DE3) *E. coli* expression system, harboring a pET11a vector containing the gene. The construction of this gene has been described previously (*9*). The S44D and S44E mutants of the chimeric thioredoxin were generated using the QuikChange site-directed mutagenesis kit from Stratagene (La Jolla, CA). The primers used for introducing the mutation were 51 base pairs long with the site for mutation at the center. *E. coli*-preferred codons were chosen for the replacement of S44 with a D or E residue. All samples were analyzed by electrospray mass spectrometry to verify the correct molecular mass. ^{15}N-labeled proteins were prepared by growing cells in minimal medium supplemented with $^{15}NH_4Cl$ as the sole nitrogen source. The ^{13}C- and ^{15}N-labeled protein was prepared by supplementing the medium with [^{13}C]glucose in addition to $^{15}NH_4Cl$. Induction of protein expression was achieved by addition of isopropyl β-thiogalactopyranoside to a final concentration of 1 mM in midlogarithmic growth. Purification was carried out as described by Louis et al. (*9*). Samples for NMR experiments contained ~1 mM protein in 100 mM sodium phosphate buffer (pH 7.0), 20 μM EDTA, 0.02% sodium azide, and 10% D_2O.

NMR Data Acquisition. All spectra were recorded at 35 °C on Bruker DRX800, DMX750, DMX600, and DMX500 spectrometers equipped with triple-resonance, triple-axes gradient probes. $^{1}H-^{15}N$ HSQC spectra were also acquired at lower temperatures in an effort to assign residues 2 and 33. Several backbone assignments were obtained by comparing $^{1}H-^{15}N$ HSQC spectra of the hybrid protein with those of the wild-type *E. coli* and human proteins. Backbone assignments were confirmed using three-dimensional (3D) HNCACB and 3D HNCO experiments (*18*). Side chain assignments were obtained from ^{15}N TOCSY-HSQC, HCCH-TOCSY, H(CCO)NH-TOCSY, and C(CO)NH-TOCSY experiments (*18*−*22*). NOE assignments were obtained from ^{15}N NOESY-HSQC and four-dimensional (4D) ^{13}C NOESY experiments (*23*). *J* coupling values for the determination of ϕ angles were obtained from an HNHA experiment, while χ angles were calculated on the basis of data from the HNHB, HNCOCG, and HNCG experiments (*24*−*27*). HN residual dipolar couplings were measured in an IPAP experiment (*28*) carried out on a ^{15}N- and ^{13}C-labeled protein sample containing ∼5 mg/mL pf1 (ASLA Ltd., Riga, Latvia) for alignment. An identical sample containing the protein without pf1 was used to collect the reference data. Residual dipolar coupling data were also collected for ^{15}N-labeled S44D and S44E mutants of the hybrid. Relaxation data were collected on an ^{15}N-labeled sample at a single field strength (500.13 MHz) at 35 °C. Spin−lattice relaxation time constants (T_1), spin−spin relaxation time constants (T_2), and $^{15}N\{^{1}H\}$NOE values for backbone ^{15}N nuclei were measured by two-dimensional (2D) inverse-detected methods using pulse sequences described by Kay et al. (*29*). Water flip back methods were used for solvent suppression (*30*). All spectra were acquired with 1024 (HN) × 256 (^{15}N) complex points with spectral widths of 7002.801 and 1317.805 Hz in the HN and ^{15}N dimensions, respectively. Points were obtained in random order for both the T_1 and T_2 relaxation experiments using 16 transients per point and a recycle delay of 2 s. The optimum recycle delay was set to ∼3 times the T_1 value of the amide protons. The relaxation delays employed for the T_1 experiments were 16, 80, 160, 240 400, 592, 800, and 1200 ms, and those used for the T_2 experiments were 16, 32, 48, 80, 112, 160, and 240 ms. The $^{15}N\{^{1}H\}$NOE experiments consisted of two consecutively recorded experiments employing recycle delays of 8 and 5 s for the reference and NOE experiments, respectively, with 64 transients per point. A presaturation period of 3 s was employed in the NOE experiment, consisting of 135° pulses applied every 15 ms. The recycle delay that was used was selected such that it was larger than $5T_1$ for the ^{15}N nuclei (*31*). Deuterium exchange experiments were carried out on a lyophilized sample dissolved in 100 mM sodium phosphate buffer (pH 7.0) and 100% D_2O; $^{1}H-^{15}N$ HSQC spectra were recorded at suitable intervals over a period of 40 h, and the intensity of the amide cross-peaks was measured.

Data Processing and Analysis. All NMR data were processed using the nmrPipe suite of programs (*32*) and analyzed using the Pipp (*33*) package. Heteronuclear dimensions were extended by linear prediction and zero filled prior to Fourier transformation. Square cosine window functions were applied with optimized shifts to all the data sets. T_1 and T_2 relaxation time constants were estimated by fitting the intensities of the cross-peaks to a single-exponential decay curve, and uncertainties in relaxation parameters were ascertained from Monte Carlo simulations. Values for steady state NOEs were calculated on the basis of the ratio of intensities of peaks in the spectra recorded with and without proton saturation. Errors in these ratios were estimated from baseline noise in the two spectra. The inertia and diffusion tensors were calculated using programs supplied by A. Palmer (*34*, *35*). Residues manifesting steady state NOE values of <0.65, indicative of significant internal motions on the picosecond to nanosecond time scale, were not used in the diffusion tensor analysis. Similarly, residues involved in conformational exchange as judged by criteria described by Tjandra et al. (*36*) were also omitted from this analysis. ModelFree version 4.01 was used to fit the extended model free spectral density function to NMR spin relaxation data (*37*). The model selection scheme has been described previously (*38*).

Structure Calculations. NOE cross-peaks were classified as strong, medium, weak, and very weak by qualitative inspection. Upper limits for interproton distance constraints of 3.0, 3.5, 5.0, and 5.5 Å were used for these categories, respectively. For methyl protons, degenerate methylene or methyl groups, non-stereospecifically assigned methylene protons, or ring protons in aromatic rings, suitable corrections were applied using DYANA (*39*). Pseudoatoms were used only for degenerate methyl, methylene, or δ/ζ protons of aromatic rings. Backbone ϕ and ψ angle constraints were calculated using TALOS (*40*) from analyses of $^{13}C_\alpha$, $^{13}C_\beta$, $^{1}H_\alpha$, $^{13}C'$, and ^{15}N chemical shifts. Only predictions classified as "good" were used in the calculations. Ranges for dihedral angle constraints were based on errors predicted for the ϕ and ψ values by TALOS. Secondary structure elements were confirmed using CSI version 1.1 (*41*). Hydrogen bonds were used as constraints in an iterative fashion. Three criteria were used for ascertaining the presence of a *cis*-proline. Intensities of NOEs between $\alpha,\alpha_{(i+1)}$ and $N,N_{(i+1)}$ protons are much larger in a cis conformation, whereas the $\alpha,\delta_{(i+1)}$ and $N,\delta_{(i+1)}$ intensities are much stronger in the trans conformation. In addition, the C_γ shift of a *cis*-proline usually lies in the range of 19.3−27.3 ppm, and the difference in the ^{13}C chemical of the C_β and C_γ is high (typically more than 7−8 ppm) (*13*). For such prolines, the Ω angle was fixed to a value of 0° in the final runs. χ angles were fixed at common staggered rotamer values (60, −60, and 180 ± 20°) based on analyses of HNHB, HNCG, and HNCOCG spectra. These spectra along with NOE intensities were used for stereospecific assignments of β-methylene protons. Other stereospecific assignments such as α-protons of glycines and methyl protons in valines and leucines were based on NOE intensities alone. Initial structure calculations were carried out using DYANA version 1.5 (*39*). A simulated annealing protocol-conjugate gradient minimization approach was used in torsion angle space for initial structure calculations. One hundred structures were generated at each stage, and 20 conformers were analyzed for constraint violations and overall structure quality. Initial structure calculations were performed using only NOE constraints. In subsequent runs, angular constraints and hydrogen bonds were added in an iterative fashion. Hydrogen bonds present in more than 80% of the structures were used as constraints only if the involved protons could be classified as slowly exchanging, based on the deuterium exchange data. The final runs employed NOE distance

constraints, backbone angle constraints, χ angle constraints along with possible stereospecific assignments, hydrogen bonds, and HNHA coupling constants. The relative weights used for upper limits, lower limits, van der Waals constraints, torsional constraints, and coupling constants were 1, 1, 2, 5, and 0.5, respectively. The top 20 structures with the lowest target function values (average of 0.93 ± 0.24) generated from a run of 100 structures were finally refined using dipolar couplings using CNS version 1.0 (*42*). The input ensemble had backbone and side chain heavy atom pairwise rms deviations of 0.46 ± 0.07 and 1.02 ± 0.13 Å, respectively. The CNS protocol involved simulated annealing in Cartesian space using the standard CNS script "anneal" at a temperature of 1000 K and 24 000 cooling steps. The dipolar coupling force constant was ramped from 0.01 to 1.0. The refinement protocol included C_α, C_β, and H_α chemical shifts, NOE distance constraints, H-bonds, J_{HNHA} couplings, HN dipolar couplings, and dihedral angle constraints. The dihedral angle constraints generated by TALOS were used with a range twice that predicted by the program. The distance ranges for the H-bonds were between 1.5 and 2.5 Å for the HN−O distances and between 2.5 and 3.5 Å for the N−O distances. The parameters for the alignment tensor were calculated using the maximum likelihood method (*43*). The quality of the structures was analyzed using PROCHECK-NMR (*44*). Figures were generated using MOLMOL (*45*, *55*). The average minimized starting structure of the hybrid thioredoxin was used for calculation of the backbone folds of the S44D and S44E mutants. Eighty-one HN residual dipolar couplings were used for structure determination. The CNS protocol involved low-temperature annealing (100 K) followed by minimization.

Stability Studies. Denaturation studies have been previously reported for *E. coli*, human, and chimeric thioredoxin (*9*). We compared these profiles with those for the S44D and S44E mutants of chimeric thioredoxin. Circular dichroism measurements were carried out on a Jasco720 spectropolarimeter equipped with a thermostatic cell holder. Thermal denaturation was monitored by measuring the far-UV molar ellipticity at 222 nm. Data were collected as a function of temperature with a scan rate of 1 °C/min over the range of 25−80 °C on 20 μM protein samples in 10 mM potassium phosphate (pH 7.0) and 1.5 M GdnHCl. The protein concentrations were measured on the basis of the absorbance at 280 nm and were adjusted to 20 μM using an extinction coefficient of 8490 M^{-1} cm^{-1}. The samples were thermally melted in the presence of 1.5 M GdnHCl to circumvent problems associated with a pronounced slope in the baseline that is believed to arise from partial unfolding of the protein (*9*).

Fluorescence measurements were carried out on a Perkin-Elmer model LS-50B luminescence spectrometer equipped with a temperature-controlled water bath. Measurements were performed with a scan speed of 120 nm/min and data intervals of 1 nm. An excitation wavelength of 295 nm was used and the spectrum averaged over four scans. All experiments were carried out on 20 μM protein samples in 10 mM potassium phosphate (pH 7.0). GdnHCl was obtained from Pierce (Rockford, IL), and the concentration of the stock solution used for the denaturation studies was measured on the basis of refractive index measurements using an Abbe refractometer from American Optical (El Paso, TX). Curve fits for the denaturation profiles were based on nonlinear least-squares fits using Kaleidagraph version 3.08. The analysis of the unfolding curves was performed as described by Louis et al. (*9*) assuming a two-state model.

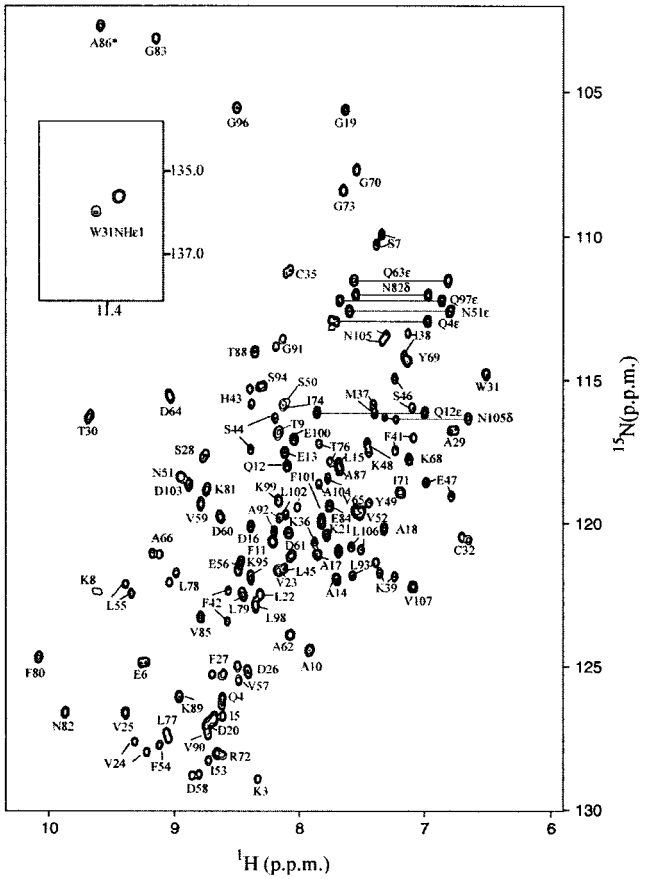

FIGURE 2: $^1H-^{15}N$ HSQC spectrum (600 MHz) of uniformly ^{15}N-labeled TRX_{HE} recorded at 35 °C in 100 mM sodium phosphate buffer, 20 μM EDTA, 0.02% sodium azide, and a 90% H_2O/10% D_2O mixture (pH 7.0). Resonances for the tryptophan indole Nϵ1H are displayed in the inset. Note the major (Met+) and minor (Met−) forms of the protein.

RESULTS AND DISCUSSION

Characterization of TRX_{HE} and Its Mutants. TRX_{HE} was expressed and purified as described in Experimental Procedures. Mass spectrometry of the uniformly ^{15}N-labeled protein revealed that the sample contained a mixture of Met(+) and Met(−) forms in a 55:45 ratio. This N-terminal heterogeneity was also reflected in a doubling of 40% of all amide resonances in the $^1H-^{15}N$ HSQC spectrum of the protein (see Figure 2). Disregarding the doubling, of the 103 expected backbone amide resonances (the protein contains four prolines), we easily identified 100. In addition, all glutamine and asparagine side chain NH_2 groups and the W31Nϵ_1H resonances were detected and assigned. Missing amide resonances were those of residues 1, 2, and 33 at 35 °C (or 10 °C) and the N_ϵ and N_ζ proton resonances of R72, presumably due to fast exchange with the solvent. The $^1H-^{15}N$ HSQC spectra of the two S44 mutants exhibited features similar to those of the hybrid protein and revealed identical peak positions for 75% of all residues (data not shown), indicating that the mutant proteins had the same overall fold. Interestingly, the minor chemical shift differences that were

observed for each of the mutants when they were compared to TRX_{HE} were not confined to the α_2 and α_4 helices, but were also propagated further, affecting backbone resonances of residues in strands β_2, β_4, and β_5. Comparing the $^1H-^{15}N$ HSQC spectra of the two mutants, S44D and S44E, revealed differences in the backbone amide resonances for I38, F41, S44, L45, S46, E47, K48, S50, L93, and L94. Thus, these changes were confined to residues in the α_2 helix around the mutation site, and to two other residues also close in space to the site of mutation (L93 and K95), at the N-terminal end of the α_4 helix.

Resonance Assignments and Secondary Structure. Almost complete ^1H, ^{15}N, and ^{13}C assignments were obtained for the human−*E. coli* thioredoxin (TRX_{HE}) at 35 °C with a relatively small set of experiments (described in detail in Experimental Procedures). The residues for which backbone assignments are missing were M1, V2, and G33. All assignments reported and used here pertain to the Met(+) form of the protein, although an analysis of the Met(−) form was also carried out. Similar patterns in terms of NOE connectivities and ^{13}C chemical shifts were observed for both forms, indicating that the two proteins were essentially identical in terms of structure. Assignments are available from BioMagResBank (accession code 5308). For a large number of residues, stereospecific assignments are available. Initial identification of the secondary structure elements present in TRX_{HE} was based on an analysis of the secondary chemical shifts (*41*, *46*), the relative intensities of backbone sequential NOEs, $^1H-^2H$ exchange data, and $^3J_{HNH}\alpha$ coupling constant values (*47*). A summary of these data is presented in Figure 3. CSI analysis shows the presence of three α-helices, comprising residues 8−19, 35−47, and 95−104. The α_2 helix, however, is disrupted or irregular for residues 39−41. The presence of a short helix α_3 for residues 65−68 was not predicted by this analysis, although it is present in the final structure. It should be noted that this region is the connection region between the two sequence portions with residue 66 being the transition point from the human to the *E. coli* sequence and both parent proteins contain a helix in this area. The β-sheet architecture predicted by CSI is similar to that in both parent proteins with β_1 comprising residues 5−7, β_2 residues 22−29, β_3 residues 52−58, β_4 residues 74−81, and β_5 residues 84−90. The $^1H-^{15}N$ HSQC spectra of the S44D and S44E mutants were assigned by comparison with the spectrum of the hybrid protein.

Structure of TRX_{HE}. The three-dimensional structure of TRX_{HE} was calculated on the basis of 2193 experimental constraints, comprising 1585 NOE distance constraints, 131 backbone dihedral angle constraints from the analysis of $^1H_\alpha$, $^{13}C_\alpha$, $^{13}C_\beta$, ^{13}CO, and ^{15}N chemical shifts with the program TALOS (*39*), 20 side chain χ_1 angle constraints from the analysis of the HNHB, HN(CO)CG, and HNCG experiments, 86 $^3J_{HNH}\alpha$ coupling constants obtained from the HNHA experiment, 88 hydrogen bond restraints based on $^1H-^2H$ exchange data, 89 HN residual dipolar coupling restraints, and 195 C_α and C_β chemical shifts. All experimental constraints that were used in the final structure calculations are summarized in Table 1A. Altogether, this set represents almost 21 constraints per residue and yields a highly defined structure. A family of 20 conformers and the regularized average structure were calculated, and the pertinent structural statistics are listed in Table 1B. The overall agreement of

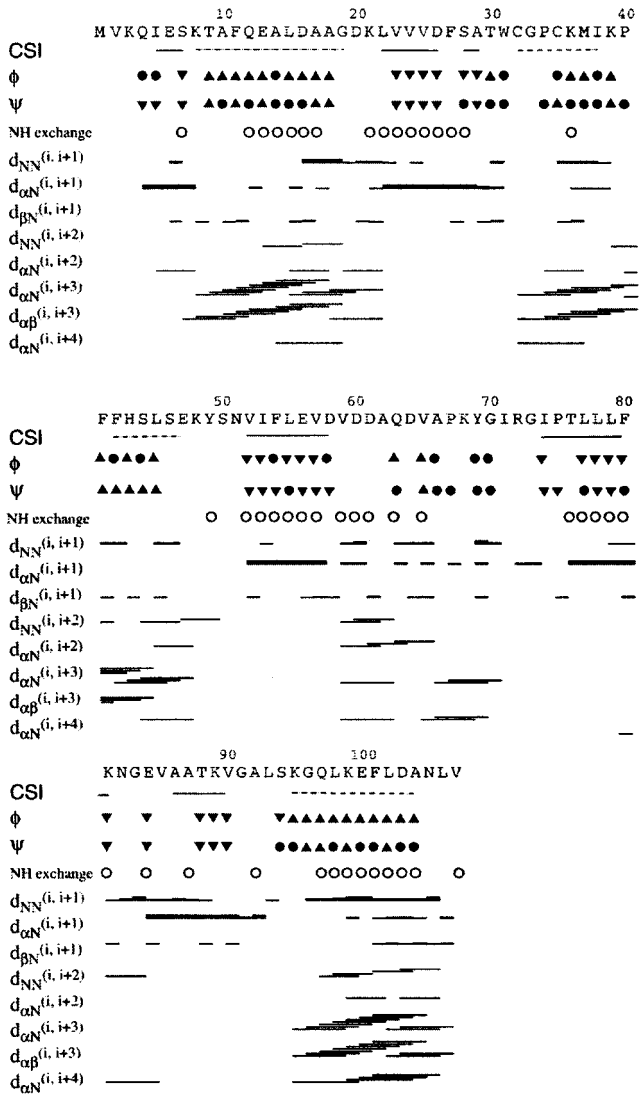

FIGURE 3: Secondary structure analysis based on deuterium exchange data, CSI, NOE connectivities, and J_{HNHA} values. CSI-derived β-sheet and α-helical elements are shown with uninterrupted and dashed lines, respectively. The ϕ and ψ angles for β-sheet and α-helical regions are represented by downward- or upward-pointing arrows, respectively, and filled circles allow either secondary structure element. Residues exhibiting slowly exchanging amide protons are represented by empty circles. The thickness of the connecting lines for the sequential NOEs qualitatively represents the intensity of the observed correlation.

the structures with the experimental data is excellent, as indicated by very small violations (no distance violations larger than 0.012 Å, no torsional violations larger than 0.36°, and no coupling constant violations larger than 0.80 Hz). The structures exhibit good covalent geometry and no van der Waals clashes (Table 1B). In addition, the high quality of the structures is reflected in good Ramachandran statistics (Table 1B). None of the non-glycine or non-proline residues are observed in the disallowed regions of the $\phi-\psi$ map. A superposition of the final ensemble of the calculated 20 conformers is shown in Figure 4A. The coordinate precision for residues 2−106 is 0.27 ± 0.06 Å for backbone atoms and 0.72 ± 0.09 Å for all heavy atoms (rms deviation of atomic coordinates with respect to the mean). Note that no constraints were used for the first residue. Most of the structure is very well defined, except the region comprising

Table 1: Structural Statistics

(A) NMR-Derived Constraints	
total no. of interproton restraints	1585
intraresidue ($i - j = 0$)	234
sequential ($i - j = 1$)	422
short-range ($1 < i - j < 5$)	348
long-range ($i - j \geq 5$)	581
no. of hydrogen bonds	88
total no. of dihedral angles	151
ϕ	64
ψ	67
χ	20
total no. of couplings constants ($^3J_{HNH}\alpha$)	86
no. of total C_α and C_β chemical shifts	195
no. of residual dipolar couplings (HN)	89
total no. of constraints	2193
total no. of constraints per residue	20.5

(B) Structural Quality	ensemble[a]	mean structure[b]
rms deviations from experimental constraints (Å)		
distance constraints	0.012 ± 0.0036	0.016
hydrogen bonds	0.014 ± 0.003	0.014
dihedral constraints (deg)	0.364 ± 0.065	0.44
$^3J_{HNH}\alpha$ coupling constants (Hz)	0.80 ± 0.05	0.84
$^{13}C_\alpha$ chemical shifts (ppm)	1.05 ± 0.02	1.08
$^{13}C_\beta$ chemical shifts (ppm)	1.26 ± 0.03	1.23
NH residual dipolar couplings (Hz)	0.51 ± 0.12	0.59
rms deviations from idealized covalent geometry		
bonds (Å)	0.0024 ± 0.0052	0.0027
angles (deg)	0.47 ± 0.03	0.45
impropers (deg)	0.42 ± 0.03	0.42
E_{LJ} (kcal/mol)[c]	-470 ± 29	−437.4
Ramachandran statistics[d]		
residues in the most favored region (%)	90.4 ± 1.4	92.3
residues in the additional allowed region (%)	8.7 ± 1.6	7.7
residues in the generously allowed region (%)	0.8 ± 0.6	0.0
residues in the disallowed region (%)	0.0	0.0
no. of bad contacts[e]	1.5 ± 1.3; 0 ± 0	2; 0

(C) Coordinate Precision	
backbone atoms (Å)	0.26 ± 0.07,[f] 0.27 ± 0.06[g]
all non-hydrogen atoms (Å)	0.71 ± 0.08,[f] 0.72 ± 0.09[g]

[a] Twenty structures. [b] Regularized mean structure. [c] E_{LJ} was calculated using parameters included in CNS parameter file for NMR calculations. [d] Calculated by PROCHECK for the ordered region (residues 3−71 and 75−106). [e] Calculated by PROCHECK; on the basis of CNS criteria (1.6 Å cutoff), no bad contacts exist in the ensemble. The identity of the PROCHECK bad contacts concerns side chain and main chain C═O oxygen atoms, solely 0.1 Å below the 2.6 Å cutoff. [f] With respect to average coordinates, excluding residues 1 and 107. [g] With respect to the regularized mean structure, excluding residues 1 and 107.

residues 72−74, just after the joint in the sequence. Figure 4B shows a tube representation of the ensemble of 20 structures, with the thickness of the tube being proportional to the rms spread of the ensemble. Most of the residues with slightly higher rms spread belong to regions of increased mobility as is evidenced by our relaxation data (see below). The overall topology is identical to that of the two parent proteins, comprising a central five-stranded twisted β-sheet surrounded by four α-helices (see Figure 4C). The two helices that were not identified using CSI are irregular in the final structures. Helix α_2 contains a kink due to the presence of P40, and helix α_3 is irregular and not well formed. This is similar to observations for the NMR structure of *E. coli* TRX that contains an α_3 helix shorter than that of human TRX. A comparison between the solution structures of human, *E. coli* (*4*, *5*), and TRX_{HE} reveals pairwise backbone rms differences of 1.45 and 0.84 Å for the human portion (residues 1−66) and the *E. coli* portion (residues 67−107) of the structure, respectively. This indicates that structural perturbations in both domains are very low, with the *E. coli*-derived domain being minimally affected. A backbone superposition of all three structures is provided in Figure 4C, and pertinent data for the structural comparison are given in Table 2. The regions that show distinct differences are the active site residues (residues 30−34), the turn connecting β_4 and β_5, and the transition point near residues 67 and 68. The rms difference between the human and the hybrid protein for residues 1−29 and 35−66 is 1.29 Å and, similarly, between *E. coli* and the hybrid for residues 69−107, excluding residues 82 and 83, is 0.63 Å. The active site residues spanning W31−C35 pack against the rest of the protein molecule in a manner that is more similar to the *E. coli* NMR structure than to the human NMR structure. It should be noted, however, that the hybrid structure is very similar in these regions to the human X-ray structure (rms difference for the backbone atoms of residues 1−66 of 0.98 Å) (*8*). The close similarity in the active site loop between the X-ray structure of human TRX, the NMR structure of *E. coli* TRX, and the structure of TRX_{HE} supports the suggestion that the M74T mutation present in the human

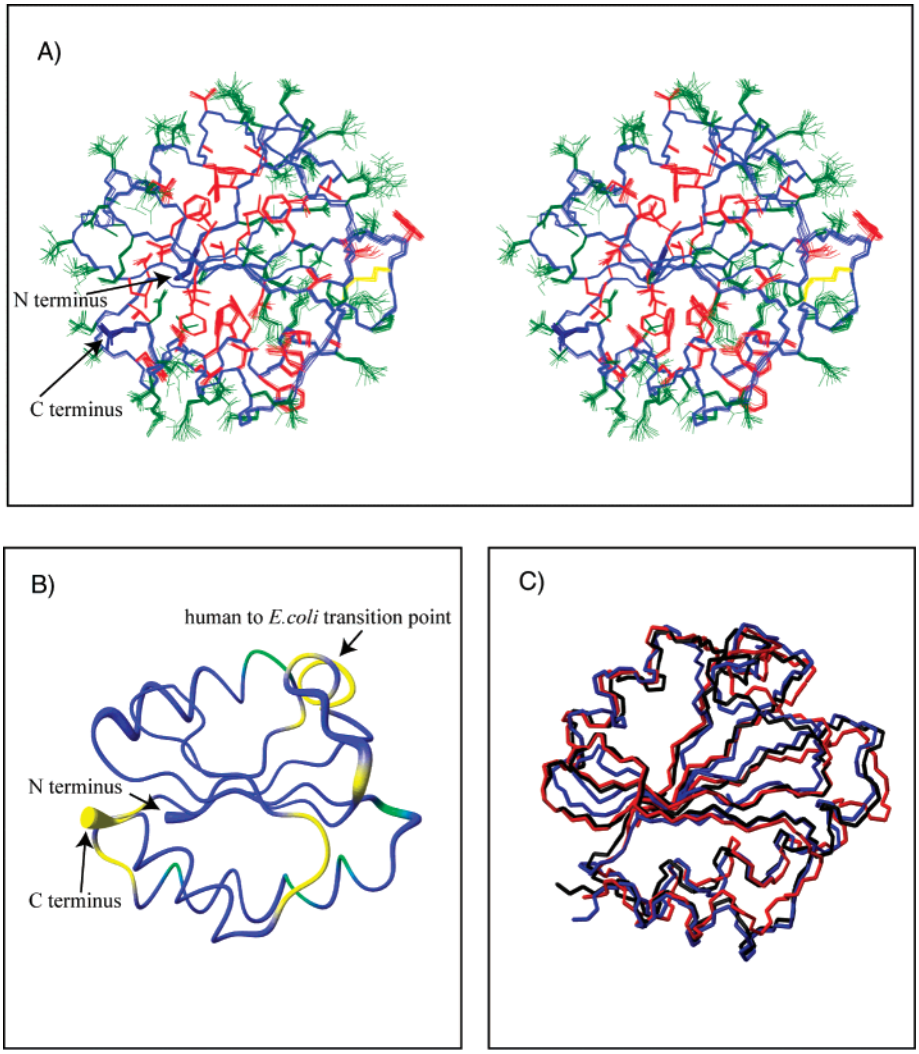

FIGURE 4: Overall structure of TRX_{HE}. (A) Stereoview showing superpositions of the final ensemble of 20 conformers of the hybrid human−*E. coli* thioredoxin (residues 2−106). The backbone (N, C_α, and CO) atoms are shown in blue, side chains with well-defined conformations in red, and others in green, and the disulfide bridge is shown in yellow. (B) Schematic representation of the backbone precision of the calculated structures and associated flexibility. The diameter of the tube is proportional to the atomic rms spread of the backbone atoms, and the motional properties are color-coded. Residues with backbone amide heteronuclear NOEs of <0.65 are colored yellow, those involved in conformational exchange green, and others blue. (C) Best fit superpositions (SwissPdb Viewer version 3.7) of the human (red), *E. coli* (blue), and hybrid (black) structures.

Table 2: Pairwise Comparison between TRX_{HE} and the Human and *E. coli* Structures

	human[a]	*E. coli*[b]
residues 4−66	1.42 Å	–
β-sheet residues (5−7, 22−29, and 52−58)	0.84 Å	–
α-helix residues (8−18, 35−48, and 62−67)	1.35 Å	–
α-helix residues (8−18 and 35−48)	1.22 Å	–
residues 67−105	–	0.72 Å
β-sheet residues (74−81 and 86−90)	–	0.45 Å
α-helix residues (95−104)	–	0.22 Å

[a] Versus the average minimized NMR human structure 1TRS (*4*). [b] Versus the average minimized *E. coli* NMR structure 1XOA (*5*).

protein used for the determination of the solution NMR structure caused a loss of favorable hydrophobic contacts between residues 73−75 and the active site loop.

Other features of the active site also seemed to be conserved between the different structures. For example, the conformation of the Cys32−Cys35 disulfide bond is similar in all the three structures and is found in a right-handed conformation. The χ_1 angle of C35 was −67.5° (39.2° for the human NMR structure −63.5° for the human X-ray structure and −59.5° for the *E. coli* NMR structure), and χ_1 for W31 in the hybrid is 59.7° (61.8° for the human NMR structure, 49.6° for the human X-ray structure, and 49.7° for the *E. coli* NMR structure). The imidazole ring of H43 in the hybrid protein is the neutral $N_{\delta 1}H$ tautomer, based on analyses of long-range $^1H-^{15}N$ HSQC data (*48*). This implies that the pK_a value has to be similar to that observed in the human protein (*4*).

As illustrated in Figure 4A, the two halves of the chimera are well-packed and the β_2 and β_4 strands form a surprisingly tight interface, despite the lack of an optimized complementarity for hydrophobic interdigitation. The remainder of the side chain conformations and interactions within the individual domains are largely preserved and unaltered from the parent molecules within the precision of the ensemble.

Residual NH dipolar couplings were employed to determine the backbone folds of the S44D and S44E mutants as described in Experimental Procedures. For both mutant proteins, the folds were very similar to that of the hybrid

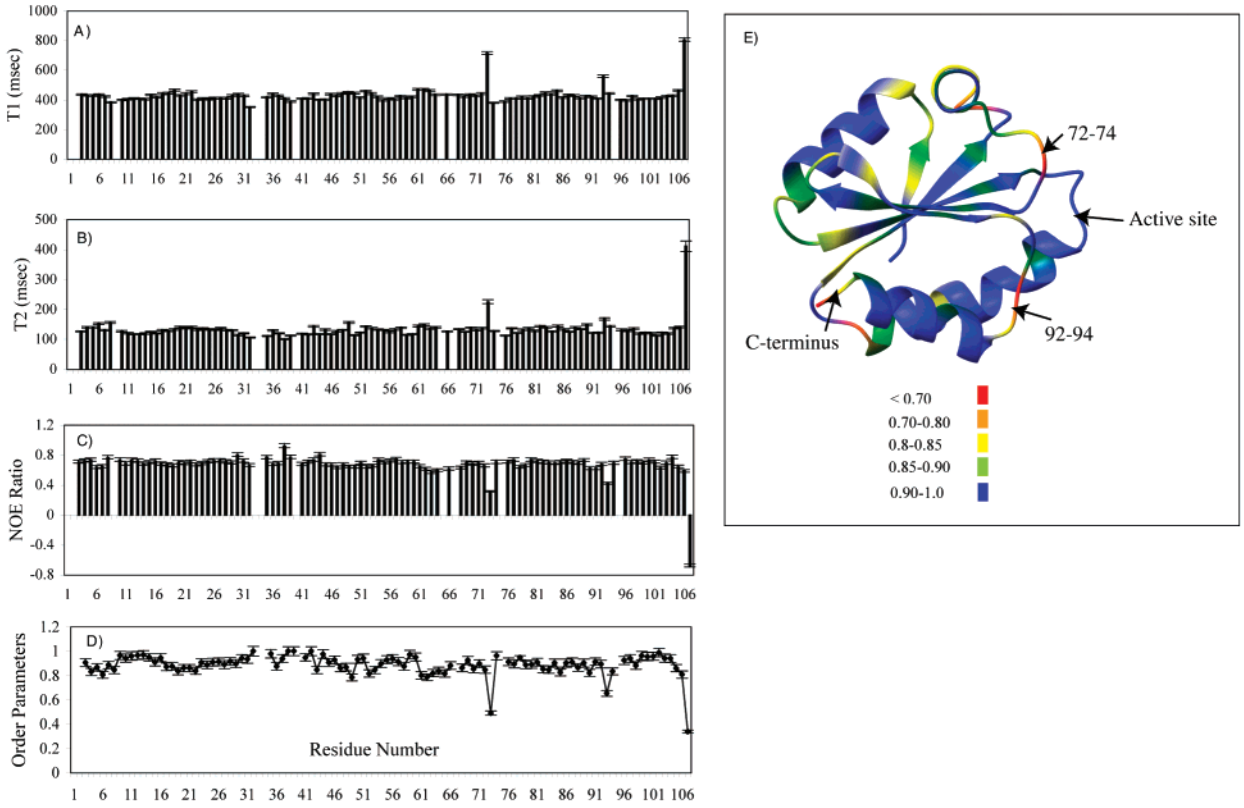

FIGURE 5: Graphical representation of ^{15}N relaxation data of human−*E. coli* thioredoxin and analysis. (A) Longitudinal relaxation times (T_1), (B) transverse relaxation times (T_2), (C) $^{15}N\{^1H\}$ NOEs, and (D) S^2 values are plotted as a function of residue number in the protein sequence in individual panels from top to bottom. In panel E, a ribbon diagram of the average minimized NMR structure is color-coded according to the order parameters.

Table 3: Rotational Diffusional Analysis of TRX_{HE}[a]

model	D_{iso} ($\times 10^{-7}$ s^{-1})	$2D_{zz}/(D_{xx}+D_{yy})$	D_{xx}/D_{yy}	θ (deg)	ϕ (deg)	Ψ (deg)	χ^2	F
isotropic	2.94 ± 0.01						191.49	
axial (oblate)	2.94 ± 0.01	0.88 ± 0.01		1.65 ± 0.12	0.67 ± 0.09		137.09	8.60
axial (prolate)	2.95 ± 0.01	1.12 ± 0.02		0.95 ± 0.08	2.27 ± 0.14		151.29	5.76
anisotropic	2.95 ± 0.01	1.10 ± 0.02	0.90 ± 0.02	1.34 ± 0.33	2.28 ± 1.50	1.56 ± 1.14	131.19	1.42

[a] The diffusion analysis was carried out for 72 amide vectors as described in Experimental Procedures. Values are reported for the optimal fit, and errors have been estimated from the covariance matrix or from Monte Carlo simulations. θ, ϕ, and ψ are the Euler angles and describe the rotation necessary for the diffusion tensor to coincide with the inertia tensor of the molecule. χ^2 is the sum squared error, describing the goodness of fit, and the F value is used to assess the statistical significance of using a more complex model (larger number of parameters) to describe the system.

protein. The backbone rms difference between the mutants and the hybrid ranged from 0.4 to 0.6 Å.

Backbone Mobility. The dynamic properties of TRX_{HE} were examined by measuring ^{15}N relaxation data as described in Experimental Procedures. The T_1, T_2, and steady state NOE values are displayed in Figure 5. Data were obtained for 100 residues of 107 total (missing data pertain to the four prolines and three unassigned residues). Residues 9, 20, 23, 45, 52, 65, 72, and 95 were eliminated from the analysis because of resonance overlap. For the most part, a uniform distribution for all measured parameters is observed. Residues 6, 49, 50, 62−64, 66, 68, 73, 78, 90, 91, 93, 106, and 107 exhibited NOE values of <0.65, and residues 8, 30, 35, 38, and 46 seemed to be involved in conformational exchange processes (*36*). This feature is consistent with the increased rms spread in the structural ensemble (see Figure 4B). All these residues were eliminated from the diffusion tensor analysis. Seventy-two of the 103 possible backbone ^{15}N relaxation parameters were used for calculation of an appropriate descriptive model for the protein using the quadric diffusion program (*34*, *35*). The extracted parameters are listed in Table 3. As can be appreciated from the results, an axially symmetric model is the best descriptor of the system, with an F statistic of 8.59, a p value of ≪0.01, and a τ_m value of 5.65 ns. A fully anisotropic model was ruled out on the basis of statistical criteria. Generally, a p value of <0.01 is considered to be statistically significant (*35*). The ModelFree analysis of the spectral density function was used with an axially symmetric model as an adequate descriptor. Most of the residues were seen to fit model 1. A few more were fit to model 2 (S^2 and τ_e). None of the residues could be described by model 3, 4, or 5. The S^2 values obtained from this analysis are shown graphically in Figure 5D and pictorially in Figure 5E. The average S^2 value for the entire protein was 0.88, indicating a rigid protein backbone. Residues exhibiting lower S^2 values include G73, L93, and V107. Both G73 and L93 are located in loops and display motional behavior similar to that observed in the *E. coli* protein (*49*). Both these residues are

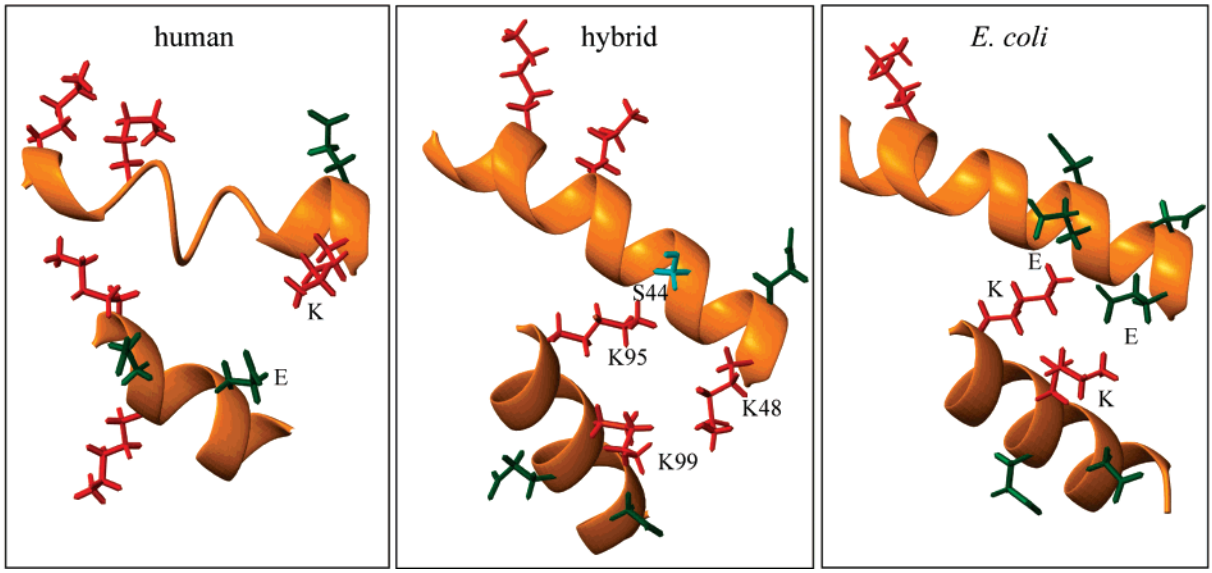

FIGURE 6: Interactions between residues on helices α_2 (long helix) and α_4 (shorter helix) in human, hybrid, and *E. coli* thioredoxins. Positively charged residues are shown in red and negatively charged ones in green. The side chain for Ser44 is shown in cyan.

known to pack against the active site of thioredoxin (residues 31−35), and mobility in this region is believed to be important for binding to different substrates and activity. Interestingly, the two new interfaces in the human−*E. coli* chimera, involving β_2 and β_4 and $\alpha_2-\alpha_4$, did not exhibit increased mobility compared to the main body of the protein. All relaxation parameters (T_1, T_2, NOE, S^2, and τ_e values) are supplied in the Supporting Information (Supplementary Table 1).

Stability of Mutants. The two mutants S44D and S44E were designed with the aim of increasing the stability of the hybrid protein. Examining the human and *E. coli* structures revealed electrostatic interactions between amino acids located on helices α_2 and α_4, and we reasoned that these may contribute to the overall stability of the protein. Although, in general, protein stability arises due to cumulative effects, contacts between the C-terminal helix and the core of the protein were previously shown to be important in thioredoxin (*7*, *11*). In the *E. coli* structure, we noticed a potential salt bridge between E44 and K96 and between E48 and K100 (see Figure 6C). In the human structure, there is an electrostatic interaction between K48 and E98 (Figure 6A). For the hybrid, no such interaction is observed. On the contrary, an unfavorable repulsive interaction is likely due to the proximity of the two positively charged side chains of K48 and K99 (Figure 6B). We therefore aimed to alleviate this repulsion by introducing a negatively charged amino acid. The position of the negatively charged residue on α_2 was chosen such that the carboxylate group of either aspartate or glutamate would be able to contact the ϵNH_3^+ group of K95 in helix α_4. Position 44 was the best site. The stabilities of the hybrid and the S44D and S44E mutant proteins were probed by fluorescence spectroscopy, and the corresponding denaturation profiles are displayed in Figure 7A. As anticipated, the mutations resulted in a change in the unfolding curves. The free energies of unfolding in the absence of denaturant, $\Delta G^\circ_{H_2O}$, as well as their dependencies on denaturant concentration (m) were larger for both mutants than for the hybrid (see Table 4). Indeed, the m values are also higher than the one reported for human thioredoxin (2.5 kcal mol^{-1} M^{-1}) (*9*). The thermal melting curves for all three proteins in the presence of 1.5 M GdnHCl monitored by CD spectroscopy are displayed in Figure 7B. The relative T_m values of the mutants follow the trend seen in the GdnHCl unfolding studies. The ΔH_m values, which are a more accurate measure of stability than T_m values, however, are identical within experimental errors. Whereas initially surprising, these data suggest that the mutations did not alter the thermal stability of the proteins. Since a single salt bridge between the α_2 and α_4 helices would simply change the electrostatic forces in the system and thermal melting is mostly influenced by hydrophobic forces, the additional salt bridge appears to have no contribution in that regard. It simply affected the cooperative nature of unfolding in chaotropic agents.

Electrostatic Interactions and Hydrogen Bonding. The role of electrostatic interactions in stabilizing protein structures has been discussed extensively (*50*−*52*). It is believed that most of the charged residues that reside on the protein surface are crucial only for solvating the molecule. Whether this hypothesis is completely true is debatable (*53*, *54*). Nevertheless, it is interesting to note that in the *E. coli* protein a large number of electrostatic interactions are present. These include K3−D47, D9−K69, D13−K18, E44−K96, and E48−K100 interactions. The interaction between D26 and K57 involves a hydrogen bond (rather than an ionic interaction) since D26 is protonated at neutral pH. However, the D26I mutant of *E. coli* thioredoxin is more stable than the wild type, suggesting that substitution with a hydrophobic residue in the protein core is favorable in terms of the overall stability of this protein. In the human protein, many fewer electrostatic interactions (E56−K39 and K48−E98) are present and D26 seems to be close enough to S28 to be involved in a hydrogen bond with the side chain hydroxyl group. The hybrid TRX, on the other hand, seems to have only one electrostatic interaction, namely, E56−K39. The neutral D26 side chain in the hybrid does not have a hydrogen bonding partner in its proximity, which may contribute to its stability being lower than those of the human and *E. coli* proteins.

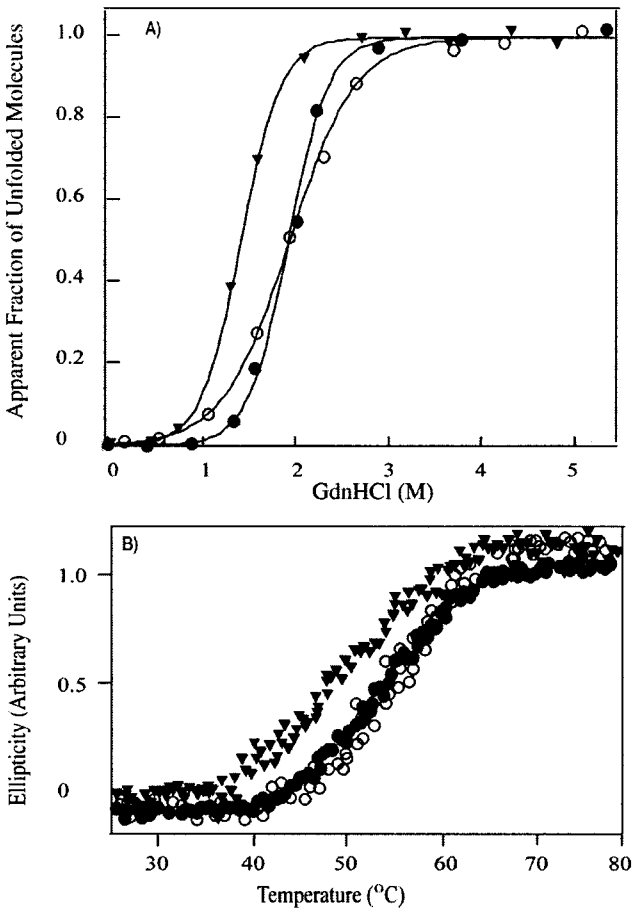

FIGURE 7: Denaturation profiles of wild-type (○), S44E (●), and S44D (▼) hybrid human−*E. coli* thioredoxin. (A) GdnHCl-induced unfolding. The (un)folding transition was followed by the intrinsic fluorescence excited at 295 nm. Raw data were converted to the fraction of unfolded molecules and plotted against GdnHCl concentration. The solid lines represent nonlinear least-squares fits of the data to the two-state model. The recovered thermodynamic parameters are summarized in Table 4. All measurements were carried out at 25 °C on samples containing 4 and 10 μM protein in 10 mM potassium phosphate buffer (pH 7). (B) Thermal denaturation curves. Unfolding was monitored with the far-UV molar ellipticity at 222 nm. Raw data were converted to the fraction of unfolded molecules and plotted against temperature. All measurements were carried out on 20 μM protein samples in 10 mM potassium phosphate (pH 7.0) and 1.5 M GdnHCl.

Table 4: Thermodynamic Parameters for the GdnHCl-Induced Unfolding of Thioredoxin Proteins

protein	C_m (M)[a]	$\Delta G°$ (kcal/mol)[b]	m (kcal mol^{-1} M^{-1})	$\Delta\Delta G_u$ (kcal mol^{-1} M^{-1})[c]
TRX_{HE}	1.9 ± 0.2	3.2 ± 0.4	1.7 ± 0.2	
S44E	1.9 ± 0.2	5.3 ± 0.6	2.8 ± 0.2	2.1 ± 0.6
S44D	1.5 ± 0.2	3.9 ± 0.6	2.8 ± 0.2	0.7 ± 0.6

[a] Concentration of GdnHCl at the midpoint of the transition. [b] Standard Gibbs free energy in the absence of denaturant. [c] Difference in standard free energy between hybrid and mutant thioredoxins.

Hydrophobic Packing. The overall packing between the various secondary structure elements was analyzed on the basis of $C_\alpha-C_\alpha$ distances between backbone atoms. For most of the secondary structure elements, these distances were comparable in all three structures. In addition, the interdomain packing was also evaluated. Primarily, there are two major "interdomain" interfaces formed, in addition to some minor interaction sites. When these interfaces are compared among all structures, no obvious factor for explaining the stability loss in the hybrid emerges. We therefore have to conclude that the loss of favorable interactions combined with subtle changes in the overall packing of the molecule is responsible for the reduced thermodynamic stability.

The main new hydrophobic core is formed by the pairing of β-strands β_2 and β_4 between residues 22 and 29 and between residues 81 and 74. The backbone geometry for the β-strands is identical to that observed in both human and *E. coli* proteins, with all hydrogen bonds intact between the two strands. The rms difference between the structures for this region is 0.26 ± 0.08 Å for the backbone and 0.60 ± 0.12 Å for the side chain atoms. Small differences among the three structures primarily arise from changed interactions between side chains, and stereoviews of this region for all three proteins are provided in Figure 8. In the hybrid, L22 interacts with K81 and L79 (see Figure 8, middle). This interaction is identical to that seen in the human protein (Figure 8, top). In *E. coli* TRX, the smaller hydrophobic chain of A22 interacts with K81 and L79. The location and packing of V23 in the hybrid are similar to those in the human protein. In *E. coli*, V23 is replaced with the bulkier I23, resulting in better hydrophobic packing with the V25 side chain. Indeed, the distance between $C_{\gamma 2}$ of I23 and $C_{\gamma 2}$ of V25 is only 3.7 Å in the *E. coli* protein. The equivalent distance between $C_{\gamma 1}$ of V23 and any C_γ of V25 in the hybrid protein is around 4 Å, and in the human protein, the closest distance between the corresponding methyl carbons is 4.6 Å. V24 in the hybrid packs against L79 instead of F79 as in the human structure. In the hybrid, the distances between $C_{\gamma 2}$ of V24 and $C_{\delta 1}$ and $C_{\delta 2}$ of L79 are 3.8 and 3.7 Å, respectively, and V24 $C_{\gamma 1}$ is more than 5 Å from the L79 side chain atoms. In the human structure, V24 is well-packed against the ring of F79, and the distances from the methyl carbons to the ring carbons are all <5 Å. In *E. coli*, L24 packs against methyl groups of both L77 and L79 (human numbering). Distances between the corresponding methyls are <5 Å. In the human and hybrid structures, such close interactions with L77 are not present. In the hybrid, V25 packs against F80, L78, and F27 instead of F80, E78, and F27 as in the human structure. This set of interactions is not very different in the *E. coli* structure. However, packing of V25 with F27 is much better in both the *E. coli* and human structures than in the hybrid. D26 in the hybrid packs against P75 and L77, similar to the interaction in the *E. coli* system. In the human structure, there is very good packing of D26 with the ring of F77. The packing of F27 with side chains of other residues is similar in all three cases. S28 points away from the interface in the hybrid structure. In the human structure, it is very close to the carboxylate group of D26, implying a possible hydrogen bond. In *E. coli*, W28 replaces S28 and points away from the interface. In the hybrid structure, the distance between C_β of A29 and $C_{\gamma 2}$ of I74 is 5.6 Å and the distance between C_β of A29 and $C_{\delta 1}$ of I74 is 3.5 Å. In the human NMR structure, due to the mutation, I74 is replaced with T74. The distance between C_β of A29 and $C_{\gamma 2}$ of T74 is 5.9 Å. The best packing between the residues in this region is seen in the *E. coli* structure, with a distance between A29 C_β and I74 $C_{\delta 1}$ of 3.4 Å (human numbering). The intrastrand interactions within the stretch of residues 74−81 are also not perturbed significantly in the hybrid in comparison with the human and *E. coli* structures.

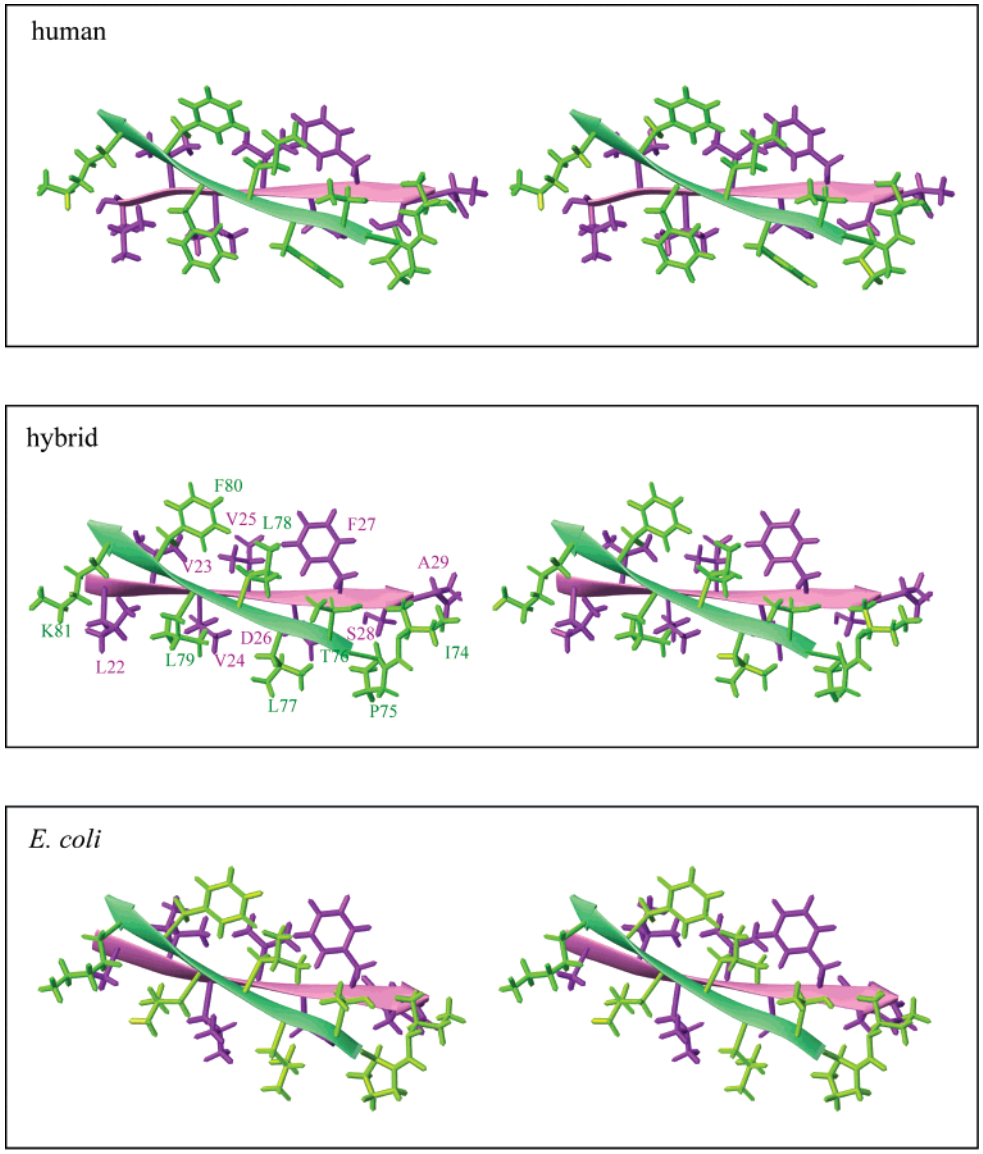

FIGURE 8: Stereorepresentation of the side chain packing for residues on strands β_2 (magenta) and β_4 (green) in human, hybrid, and *E. coli* thioredoxins. Amino acids in the hybrid structure are labeled by residue name and numbers.

At this point, it is important to emphasize that even if the interactions between the two domains may seem to be well-optimized in the hybrid, slight imperfections could clearly be present both in the newly created interface and within the individual domains. The net stabilization of the protein would therefore be determined by the interplay between these two effects.

The other new interface that has a significant surface area of interaction is made up of α_2 (residues 34−47) and α_4 (residues 92−106). The favorable interactions in the hybrid include methyl−methyl interactions between L45 and L102, L98, and A92 with P34. Some unfavorable interactions include the proximity of positive charges on K99 and K48. In the human structure, one observes a possible salt bridge between K48 and E98 as discussed above and also a larger number of hydrophobic interactions. L48 interacts with I101, F41 with K94, F42 with L97, I38 with A92, and I38 with K94. In the *E. coli* structure, the ionic interactions discussed above and hydrophobic interactions between I41 and L97, L42 and L97, and I38 and A92 (human numbering) are present.

Furthermore, packing between the active site and the loops containing residues 92 and 74 is important. The active site residues in the hybrid pack better against the loop containing I74 than in the human NMR structure, thus adopting a packing geometry similar to that in the *E. coli* structure. For example, the closest distance between any two heavy atoms of W31 and T74, in the human NMR structure, is 7.3 Å. However, in the human X-ray structure, the W31 ring is quite close to M74, with the shortest distance between heavy atoms of these residues being 3.6 Å. In the case of the hybrid structure, the shortest distance between W31 and I74 heavy atoms is 4.4 Å. Similarly, the distance between C_β of P34 and C_β of A92 in the hybrid is 4.4 Å, while this distances are 5.1, 8.5, and 3.9 Å in the *E. coli*, human NMR, and human X-ray structures, respectively. This implies that substitution of a threonine residue for a methionine residue in the human thioredoxin significantly decreases the extent of hydrophobic contact between the active site and the loops around residues 74 and 92. More specifically, the substantially longer side chain of methionine compared to that of threonine allows the methyl group to move much closer to

other hydrophobic residues. We therefore conclude that the differences previously observed between the NMR and X-ray structures of human thioredoxin in this region are essentially caused by the M74T mutation, rather than reflecting real differences between the solution and crystal states.

A further minor difference involves L22. In the hybrid, the L22 methyl groups do not interact with those of L106. In the *E. coli* structure, very good packing between these residues is seen. No significant differences are observed for residues 65−69 that form the helix at the transition point from the human to *E. coli* sequences. A new electrostatic interaction between D64 and K68 is formed, and good hydrophobic packing among A62, V65, and A66 methyl groups is observed.

CONCLUSIONS

The overall structure and dynamic behavior of the chimeric human−*E. coli* thioredoxin is very similar to that of the parent proteins. Interestingly, the thioredoxin fold appears to be very resilient to changes in packing within the hydrophobic core. The most notable effect is observed for the stability of the protein, with a T_m of the hybrid of 75.7 °C, while those of the human and *E. coli* proteins are significantly higher at 91.2 and 88.7 °C, respectively (*9*). It is quite clear from the structural analysis that there is no single structural determinant that can be identified as causing the lowered stability of the hybrid. A number of features cumulatively have resulted in this property. The primary contributors are fewer salt bridges throughout the structure, specifically in the $\alpha_2-\alpha_4$ interface and suboptimal packing of the V23 and V24 side chains within the core of the molecule. Indeed, this study shows again that proteins are highly malleable and stability can easily be reduced without major structural changes.

ACKNOWLEDGMENT

We thank Dan Garrett and Frank Delaglio for software, R. Tschudin for technical support, Philippe Pelupessy for the setup of NMR experiments, and Lewis K. Pannell for mass spectrometry.

SUPPORTING INFORMATION AVAILABLE

Relaxation data for TRX_{HE}. This material is available free of charge via the Internet at http://pubs.acs.org.

REFERENCES

1. Eklund, H., Gleason, F. K., and Holmgren, A. (1991) *Proteins 11*, 13−28.
2. Katti, S. K., LeMaster, D. M., and Eklund, H. (1990) *J. Mol. Biol. 212*, 167−184.
3. Holmgren, A., Söderberg, B. O., Eklund, H., and Branden, C. I. (1975) *Proc. Natl. Acad. Sci. U.S.A. 72*, 2305−2309.
4. Qin, J., Clore, G. M., and Gronenborn, A. M. (1994) *Structure 2*, 503−522.
5. Jeng, M. F., Campbell, A. P., Begley, T., Holmgren, A., Case, D. A., Wright, P. E., and Dyson, H. J. (1994) *Structure 2*, 853−868.
6. Mittard, V., Blackledge, M. J., Stein, M., Jacquot, J. P., Marion, D., and Lancelin, J. M. (1997) *Eur. J. Biochem. 243*, 374−383.
7. Nicastro, G., De Chiara, C., Pedone, E., Tato, M., Rossi, M., and Bartolucci, S. (2000) *Eur. J. Biochem. 267*, 403−413.
8. Weichsel, A., Gasdaska, J. R., Powis, G., and Montfort, W. R. (1996) *Structure 4*, 735−751.
9. Louis, J. M., Georgescu, R. E., Tasayco, M. L., Tcherkasskaya, O., and Gronenborn, A. M. (2001) *Biochemistry 40*, 11184−11192.
10. Slaby, I., Cerna, V., Jeng, M. F., Dyson, H. J., and Holmgren, A. (1996) *J. Biol. Chem. 271*, 3091−3096.
11. Pedone, E., Saviano, M., Rossi, M., and Bartolucci, S. (2001) *Protein Eng. 14*, 255−260.
12. Yang, X. M., Georgescu, R. E., Li, J. H., Yu, W. F., Haierhan, and Tasayco, M. L. (1999) *Pac. Symp. Biocomput. '99*, 590−600.
13. Yu, W. F., Tung, C. S., Wang, H., and Tasayco, M. L. (2000) *Protein Sci. 9*, 20−28.
14. Hellinga, H. W., Wynn, R., and Richards, F. M. (1992) *Biochemistry 31*, 11203−11209.
15. Jones, S., Marin, A., and Thornton, J. M. (2000) *Protein Eng. 13*, 77−82.
16. Sheinerman, F. B., Norel, R., and Honig, B. (2000) *Curr. Opin. Struct. Biol. 10*, 153−159.
17. Tasayco, M. L., Fuchs, J., Yang, X. M., Dyalram, D., and Georgescu, R. E. (2000) *Biochemistry 39*, 10613−10618.
18. Bax, A., and Grzesiek, S. (1993) *Acc. Chem. Res. 26*, 131−138.
19. Marion, D., Driscoll, P. C., Kay, L. E., Wingfield, P. T., Bax, A., Gronenborn, A. M., and Clore, G. M. (1989) *Biochemistry 28*, 6150−6156.
20. Fesik, S. W., and Zuiderweg, E. R. (1990) *Q. Rev. Biophys. 23*, 97−131.
21. Clore, G. M., Bax, A., Driscoll, P. C., Wingfield, P. T., and Gronenborn, A. M. (1990) *Biochemistry 29*, 8172−8184.
22. Logan, T. M., Olejniczak, E. T., Xu, R. X., and Fesik, S. W. (1992) *FEBS Lett. 314*, 413−418.
23. Clore, G. M., and Gronenborn, A. M. (1991) *Science 252*, 1390−1399.
24. Vuister, G. W., and Bax, A. (1994) *J. Biomol. NMR 4*, 193−200.
25. Bax, A., Vuister, G. W., Grzesiek, S., Delaglio, F., Wang, A. C., Tschudin, R., and Zhu, G. (1994) *Methods Enzymol. 239*, 79−105.
26. Hu, J. S., Grzesiek, S., and Bax, A. (1997) *J. Am. Chem. Soc. 119*, 1803−1804.
27. Archer, S. J., Ikura, M., Torchia, D. A., and Bax, A. (1991) *J. Magn. Reson. 95*, 636−641.
28. Ottiger, M., Delaglio, F., and Bax, A. (1998) *J. Magn. Reson. 131*, 373−378.
29. Kay, L. E., Torchia, D. A., and Bax, A. (1989) *Biochemistry 28*, 8972−8979.
30. Piotto, M., Saudek, V., and Sklenar, V. (1992) *J. Biomol. NMR 2*, 661−665.
31. Farrow, N. A., Zhang, O., Forman-Kay, J. D., and Kay, L. E. (1997) *Biochemistry 36*, 2390−2402.
32. Delaglio, F., Grzesiek, S., Vuister, G. W., Zhu, G., Pfeifer, J., and Bax, A. (1995) *J. Biomol. NMR 6*, 277−293.
33. Garrett, D., Powers, R., Gronenborn, A. M., and Clore, G. M. (1991) *J. Magn. Reson. 95*, 214−220.
34. Lee, L. K., Rance, M., Chazin, W. J., and Palmer, A. G., III (1997) *J. Biomol. NMR 9*, 287−298.
35. Bruschweiler, R., Liao, X., and Wright, P. E. (1995) *Science 268*, 886−889.
36. Tjandra, N., Kuboniwa, H., Ren, H., and Bax, A. (1995) *Eur. J. Biochem. 230*, 1014−1024.
37. Palmer, A. G., Rance, M., and Wright, P. E. (1991) *J. Am. Chem. Soc. 113*, 4371−4438.
38. Mandel, A. M., Akke, M., and Palmer, A. G., III (1995) *J. Mol. Biol. 246*, 144−163.
39. Güntert, P., Mumenthaler, C., and Wüthrich, K. (1997) *J. Mol. Biol. 273*, 283−198.
40. Cornilescu, G., Delaglio, F., and Bax, A. (1999) *J. Biomol. NMR 13*, 289−302.
41. Wishart, D. S., and Sykes, B. D. (1994) *J. Biomol. NMR 4*, 171−180.
42. Brunger, A. T., Adams, P. D., Clore, G. M., DeLano, W. L., Gros, P., Grosse-Kunstleve, R. W., Jiang, J. S., Kuszewski, J., Nilges, M., Pannu, N. S., Read, R. J., Rice, L. M., Simonson, T., and Warren, G. L. (1998) *Acta Crystallogr. D54*, 905−921.
43. Warren, J. J., and Moore, P. B. (2001) *J. Magn. Reson. 149*, 271−275.
44. Laskowski, R. A., Rullmannn, J. A., MacArthur, M. W., Kaptein, R., and Thornton, J. M. (1996) *J. Biomol. NMR 8*, 477−486.

45. Koradi, R., Billeter, M., and Wüthrich, K. (1996) *J. Mol. Graphics 14*, 51−55.
46. Wishart, D. S., and Sykes, B. D. (1994) *Methods Enzymol. 239*, 363−392.
47. Wüthrich, K. (1986) *NMR of Proteins and Nucleic Acids*, Wiley, New York.
48. Clore, G. M., Bax, A., Wingfield, P., and Gronenborn, A. M. (1988) *FEBS Lett. 238*, 17−21.
49. Stone, M. J., Chandrasekhar, K., Holmgren, A., Wright, P. E., and Dyson, H. J. (1993) *Biochemistry 32*, 426−435.
50. Argos, P., Rossman, M. G., Grau, U. M., Zuber, H., Frank, G., and Tratschin, J. D. (1979) *Biochemistry 18*, 5698−5703.
51. Scandurra, R., Consalvi, V., Chiaraluce, R., Politi, L., and Engel, P. C. (1998) *Biochimie 80*, 933−941.
52. Scandurra, R., Consalvi, V., Chiaraluce, R., Politi, L., and Engel, P. C. (2000) *Front. Biosci. 5*, D787−D795.
53. Kumar, S., Ma, B., Tsai, C. J., and Nussinov, R. (2000) *Proteins 38*, 368−383.
54. Kumar, S., and Nussinov, R. (2001) *Cell. Mol. Life Sci. 58*, 1216−1233.
55. Koradi, R., Billeter, M., and Wüthrich, K. (1996) *J. Mol. Graphics 14*, 29−32.

BI0258501